

# N-body Galaxy Simulation Using Barnes-Hut Algorithm

Andrew Thompson, Shawn Knabel, Travis Waters<sup>1</sup>

<sup>1</sup> *University of Louisville, Department of Physics and Astronomy, 102 Natural Science Building, 40292 KY Louisville, USA.*

Accepted XXX. Received YYY; in original form ZZZ

## ABSTRACT

We model the overdensities in the intergalactic medium of deep space in a large volume in order to simulate the formulation of a galactic structure in an N-body gravitational system utilizing a Barnes-Hut algorithm over the span of five billion years. We initialize the simulation with a variety of values for rotational and randomized velocities for each uniformly distributed, unit-mass objects and observe the resulting motion and morphological structure. The evolution and structure of the objects are measured by the relation of the structure's energy to the Virial theorem, and the radial distribution of the mass to accepted observations. The goal is to understand the effects of initial conditions on the resulting structure (e.g. disk formation, spiral arms, mass distribution, etc.) over significant time scales under gravitational forces alone.

**Key words:** Galaxies – N-body simulations – disk galaxies

## 1 INTRODUCTION

Galaxies form from overdensities in the mass distribution of a region of space, where gravity forces the accumulation of matter into larger structures. Modern cosmological theory suggests that these overdensities coincide with halos of dark matter that influence the initial conditions of the baryonic matter prior to collapse. Hierarchical structure formation has been thought to result from a singular collapse of a large gas cloud, with smaller structures forming later (Eggen et al. (1962)). More widely accepted theories postulate that smaller clumps of matter within dark matter halos merge to form the galaxies, groups and clusters (White (1976), White & Sharp (1977)). Modern theories still struggle to precisely determine the mechanism which halts the collapse. In either model, the initial angular momentum is conserved throughout gravitational collapse, and the resulting shape of the structure depends to a large extent on this principle.

Edwin Hubble's morphological classification scheme (Hubble (1926), Hubble (1927)) divides galaxies based on their appearance into three main classes: elliptical, spiral, and irregular. This classification scheme is traditionally presented in a tuning fork shape. Hubble emphasized that this diagram was meant to show empirical classification with no statement regarding temporal evolution of what he referred to as "nebulae," which we now call galaxies. Despite this, elliptical galaxies are often referred to as early-type galaxies, even though much evidence shows them to be the end-product of galaxy evolution. Observational constraints show that the modern cosmological Cold Dark Matter ( $\Lambda$ CDM) model robustly describes the story of galaxy evolution to "red and dead" (lacking star-formation) elliptical galaxies (De Lucia et al. (2006)). Spiral galaxies, which are often referred to as late-type galaxies, are in fact shown to possess significantly more gas and therefore star-formation, strongly suggesting that the nomenclature of "early-

type" and "late-type" are fatal misnomers. Observation of the earliest galaxies, such as those produced by the Hubble Deep Field and HST eXtreme Deep Field (Williams et al. (1996), Illingworth et al. (2013)) at high redshifts, has begun to reveal some of the structures of early galaxy formation, showing irregular and disk galaxies to be the earliest structures formed.

The conservation of angular momentum interacting with the mass within the galaxy and with other nearby galaxies causes different morphologies to develop over time. Recognized classifications include elliptical shaped galaxies, spiral shaped with disks with bars and spiral arms. Hubble classified spiral galaxies according to the size of their central bulge, the profile of the spiral arms (tightly or loosely bound), and amount of gas and dust. The scheme goes Sa, Sb, and Sc in order of big, tight, little gas to small, loose, lots of gas. Spiral galaxies with central bars are designated as SBa, SBb and SBc instead. The gas-rich spiral arms are the environments in which a young galaxy begins to ignite its first stars. The shapes formed, and the time it takes for these shapes to form, must depend to some extent on the initial conditions of the mass distribution and velocities. The conditions that lead to early structures deep in our universe is of prime importance to modern cosmology.

Deep field observations provide evidence for comparison against simulations, and together they can afford an insight into the nature of the early intergalactic medium and the initial process of galaxy formation.

## 2 N-BODY SIMULATIONS

N-body simulations are used to study the dynamical physics of large numbers of objects distributed over a region of space. With a large number of bodies  $N$ , this can begin to model a more continuous distribution of matter, charge, etc. Gravitational simulations are

particularly straightforwardly conducted using N-body simulations because the force between objects is easily modeled by an inverse square proportionality. The first gravitational N-body simulations were conducted by Erik Holmberg in 1941 to study the tidal effects on the stars of galaxies passing at a close distance (Holmberg (1941)). Using an analog system of lightbulbs and the inverse square proportionality of light propagation, the gravitational force on each body is modeled by the flux from each lightbulb measured by a photocell at the stars' positions. Modern simulations make use of the computational power of computers to solve the equations of motion for each object in the study. At each timestep, the superposition of all gravitational forces on each object by every other object is calculated, and the resulting displacement is instantaneously executed, representing the motion of the distribution over the time period determined by the input parameter of the step length. This calculation, while simple, is computationally taxing for large N. This requires novel approximations to reduce run-time.

The Barnes-Hut algorithm, introduced by Josh Barnes and Piet Hut (Barnes & Hut (1986)), is a clever method for alleviating the computational weight of each step of the simulation. It is an example of a tree method, which uses an octree to divide the three-dimensional volume into smaller cubic cells. The cells of the octree, called nodes, are subdivided until each body is contained within its own subdivision. Nodes that contain further subdivisions (i.e. contain more than one body) are called *internal nodes*, and they store the information from all their subdivisions as a collective total mass and center of mass. The bottom level of subdivisions, which are empty or contain only one body, are called *external nodes*. Nodes are divided into smaller cells for denser regions. In this system the contributions of gravitational force from individual bodies on a single test body is calculated only for those that are sufficiently close. The algorithm begins with the root node, representing the entire region of space, and works through the internal nodes, treating contributions from entire nodes as a single force from the center of mass of that cell instead of summing the contribution of each individual object. For each node, the ratio of the width of the cell to the distance from the test body to the node's center of mass  $w/d$  is compared to an input parameter  $\theta$  to determine whether the algorithm considers smaller subdivisions. If the internal node is sufficiently close (i.e.  $w/d < \theta$ ) then the algorithm continues to the next layer of subdivisions. This greatly reduces the number of pair interactions to be computed in each step, reducing computational cost.

An example of the tree generated by the Barnes-Hut algorithm is shown in Figure 1. The entire simulation space containing 23 bodies on the left hand side is represented by the root node of the tree on the right hand side. We then subdivide the root cell into four cells of equal size and mark how many particles are in each region. The focus in this example is on the bottom left cell. We continue subdividing each new cell until at most one particle remains. Each node in the tree also calculates the center of mass of all particles contained within for use in force calculations. While this example is in only two-dimensions, it is easily applied to a three-dimensional oct-tree by subdividing each cell into eight cells of equal size instead of four.

### 3 OUR ALGORITHM

Our simple model considers only the effects of gravity, and therefore does not take into account the complex physics that are introduced by the presence and evolution of stars. Stellar feedback processes

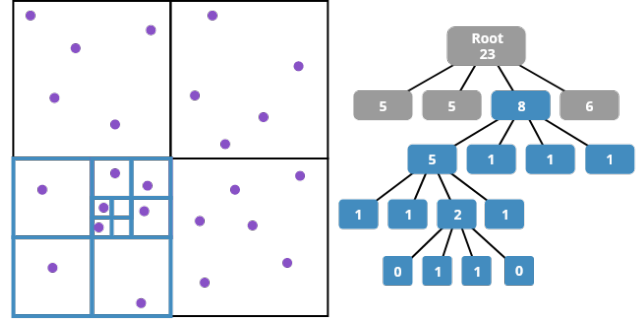


**Figure 1.** An example two-dimensional Barnes-Hut quad-tree

would introduce additional complexities that are better modeled by hydrodynamical simulations that are outside the scope of this project. In order to quantify the connection between the early structure formation and the initial velocities of the bodies involved, we focus on the dynamics and kinematics of systems of N-bodies distributed in three-dimensional space.

The structure of the algorithm is adapted from the Barnes-Hut algorithm and closely follows its model. Each step of the simulation, an updated tree is constructed for use in gravitational force calculations, from which velocities and positions of each body can be derived. Only a single thread is used per simulation to avoid the complexities of parallel computing. Some extra steps were taken, however, to improve single threaded performance and efficiency.

Input parameters to the simulation include the number of bodies, the number of 0.0001 Gyr time steps, the initial total rotational velocity (in rad/Gyr), and the mean randomized velocity (in km/s). The process of initialization will be discussed in more detail in Section 4.2. For  $\theta$  to be used in the Barnes-Hut algorithm when determining whether an approximation is appropriate, we chose the common value of  $\theta = 1.0$ .

#### 3.1 Memory Layout

Positions and velocities were stored as contiguous arrays of three double precision floating point numbers, one for each axis. Cells were also stored as a contiguous array. To conserve memory as much as possible, the cells array started with only the capacity to store one cell, and doubled in capacity only when needed. Crucially, the eight sub-cells that share the same direct parent cell are all stored next to each other in memory. These data patterns ensure that pertinent data is tightly packed together, a quality which modern processors enjoy due to their pre-fetching abilities. When iterating through a cell's sub-cells, as is often done, it is likely that the next sub-cell needed will already be in the processors cache. This contrasts the alternative method of storing cells, a linked list, where each access to a cell's sub-cells would involve the chasing of a pointer to an essentially random memory location, which can not take advantage of the processor's much faster cache.

#### 3.2 Recursion

Much of the Barnes-Hut algorithm's can be achieved through recursion, providing an elegant way of tackling the problem. This recursive pattern was used when adding bodies to cells, recursively delving deeper into the tree as needed until an appropriate cell is found for a body. However, when calculating the force between a cell and a body, recursion proved to be insufficient. As more and

more recursions occur, the risk of a stack overflow is increased, an issue for simulations with many bodies and subsequently many cells. Instead, a "queue" of cells to inspect was formed on the heap, rather than the stack, to avoid this problem. Any time further precision was needed, instead of recursing deeper into the tree structure, the cell's indices were added to the queue to see if an approximation could be made on it's center of mass.

### 3.3 Artifacts

Another common issue with n-body simulations has to do with "artifacts." When two bodies get very close together, the distance between them is very close to zero, causing a massive force to be calculated. This results in an incredibly large velocity. This is not a problem when dealing with infinitely small time steps, however simulations do not get this luxury. The result is a large velocity being applied to a large time step, causing bodies to fly past one another in an unrealistic way.

While this problem has had bodies of work dedicated to it, the strategy we employed was a naive one, essentially creating a "floor" of the smallest distance allowed between bodies. This is done by introducing a "softening" factor that if the distance between the bodies is within, we assume that the distance between the bodies is the softening factor instead. Thus, the force acting on a body from a cell would be:

$$F_{\text{grav}} = \begin{cases} \frac{-GMm}{\phi^2} & \text{if } r < \phi \\ \frac{-GMm}{r^2} & \text{if } r \geq \phi \end{cases}$$

where  $G$  is the gravitational constant,  $M$  and  $m$  are the total mass of the cell and body respectively,  $r$  is the distance from the body to the center of mass of the cell, and  $\phi$  is the softening factor. This essentially dampens the force between bodies while still allowing the force to be proportional to the masses involved. The softening factor chosen was  $\phi = 0.1 \text{ pc}$ . The merits of this solution are discussed later in Section 6.4.

## 4 THE EXPERIMENT

### 4.1 Constant Parameters

To determine the size of space for uniform distribution of the mass, we approximate the average mass density of filaments in the intergalactic medium to be  $\rho_{IGM} = 1.48 \times 10^{-7} M_{\odot}/\text{pc}^3$ . The overdensities clearly should be more than this, and the initialization of the simulation with this density did not develop along timescales that reasonably simulated the growth of structure in our finite-aged universe. Therefore, we took an overdensity in the matter distribution to be an order of magnitude higher for our experiments ( $\rho_0 = 1.48 \times 10^{-6} M_{\odot}/\text{pc}^3$ ). A typical spiral galaxy contains on the order of  $M_* \sim 10^8 M_{\odot}$  of stellar matter (Ostriker et al. (1974), Sofue & Rubin (2001)), so we begin with this matter distributed over a volume that will result in the mass density  $\rho_{IGM}$ . The region of space for each simulation is then a cube of volume  $V = \rho_0/10^8 M_{\odot} = 6.77 \times 10^4 \text{ kpc}^3$  and side-length  $40.8 \text{ kpc}$ . This appears to be a reasonable spatial region considering the diameter of the Milky Way galaxy is roughly 20-30 kpc, having condensed from a larger initial volume. With a consistent amount of mass and space, the initial conditions to be varied are primarily in the systematic input parameters (i.e. number of bodies/mass per body) of the algorithm and the initial states of motion.

Number of steps	Mean $v_{rand}$ (km/s)	$\Omega$ (rad/Gyr)
25000	0	0.1 ... 0.15 ... 0.2
50000	2	0.25 ... 0.30

**Table 1.** Initialization Input Parameters.  $\Omega$  is the total angular velocity in radians per gigayear. Mean values are listed for the Gaussian distribution from which values of  $v_{rand}$  taken, with a standard deviation of 30% the mean.  $N$  is the number of bodies in the system, and the number of steps refers to the number of gigayear timesteps of the experiment.

### 4.2 Initialization Parameters

The primary parameters to be determined in the initial conditions involve the initial velocities of the bodies in the system. As long as the vector sum of these velocities includes a nonzero angular component about the axis that passes through the center of mass, there will be nonzero total angular momentum. This angular momentum stabilizes the gravitational collapse and leads to the disk structures that are of interest in this study. We thus initialize the system using values for the components of each individual object's velocity that are determined in the following way:

- (i) Total angular velocity  $\Omega$  is defined
- (ii) Each of the  $N$  bodies is assigned the average angular velocity

$$\Omega_0 = \frac{\Omega}{N}$$

- (iii) Tangential (rotational) velocity of the  $i$ -th body at position  $\mathbf{r}_i$  is calculated as

$$\mathbf{v}_{i,rot} = \mathbf{r}_i \times \Omega_0 = -y_i \Omega_0 \hat{x} + x_i \Omega_0 \hat{y}$$

- (iv) Magnitude of an additional randomized velocity component of the  $i$ -th body  $\mathbf{v}_{i,rand}$  is drawn from a Gaussian distribution
- (v) The direction of  $\mathbf{v}_{i,rand}$  is pulled from uniform distributions of altitudinal and azimuthal angles  $\theta$  and  $\phi$  where

$$v_{i,rand,x} = v_{i,rand} \sin \theta \cos \phi$$

$$v_{i,rand,y} = v_{i,rand} \sin \theta \sin \phi$$

$$v_{i,rand,z} = v_{i,rand} \cos \theta$$

- (vi) The initial velocity of the  $i$ -th body is then

$$\mathbf{v}_{0,i} = \mathbf{v}_{i,rot} + \mathbf{v}_{i,rand}$$

Table 1 shows the input parameters selected for experimentation. From the paper that Travis found, which used an initial value for  $\Omega$  of 0.16 radians per gigayear, we select a range of values from 0.1 to 0.3 in steps of 0.05 radians per gigayear. From another paper that Travis found, we chose a range of values for the mean magnitude of the velocity for the Gaussian distribution of  $v_{rand}$  at 0, 2, and 10 kilometers per second. We initialize with a modest number of bodies  $N=25,000$  in the system for the sake of computational expense. We begin with a constant total mass of  $M_{total} = 10^8 M_{\odot}$ , which is a typical size for observed disk galaxies. The mass of each body is then determined by the total mass divided by this number  $N$ ,  $M_{body} = 4000 M_{\odot}$ . We limit our analysis to the earliest stages of formations with a total number of timesteps in each simulation of  $\tau = 25,000$  and 50,000, corresponding to 2.5 and 5.0 Gyr respectively where each timestep is 0.1 Myr. We are interested in the initial formation of structure, so longer time periods are not particularly valuable for our study, given the increased computational cost.

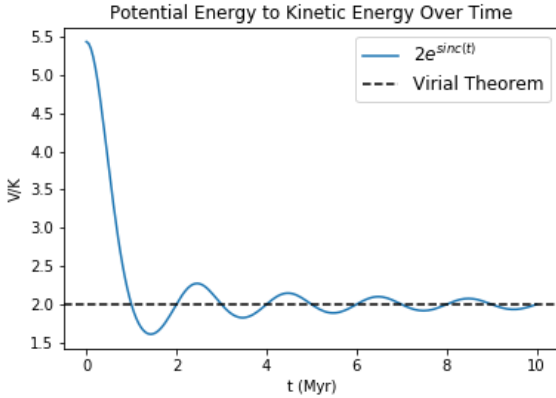


**Figure 2.** Virial Expectation

### 4.3 Energies

In order to understand the dynamics of the system, we monitor the kinetic and gravitational potential energies of the entire system at each step. The evolution of the energy of the system as the structure begins to take shape gives us insights into the mechanisms by which these structures form. For a stable, bound system of discrete bodies that obey Newton's Second Law, the virial theorem states that the time-averaged potential and kinetic energies will be proportional to each other by a factor two in a closed and gravitationally bound system.

$$\frac{\langle |U| \rangle}{\langle |K| \rangle} = 2$$

If the structure formation occurs the way we expect, then we expect the system to approach the virial condition over time. This might look something like Figure 2. For different combinations of initial conditions, the system will initiate with different values for the magnitudes of the kinetic and potential energies. We are interested to see if the initial conditions determine whether the virial condition is reached, as well as their effect on the time to reaching that state.

### 4.4 Monitoring Structure Formation and Morphology

Of primary interest is the effect of the initial conditions on the formation of disk structure, so we monitor the spatial distribution of mass throughout the space. The distribution of the absolute values each spatial coordinate ( $x, y, z$ ) for each body is analyzed at each 1000 steps (or something). Since the mass of each body is uniform, the mass density is represented by the spatial number density of bodies. Observation has shown spiral disk galaxies to radial luminosity distributions following approximately an exponential function when viewed face-on (from the axis of rotation, the  $z$ -axis) (Freeman 1970).

$$\frac{I_R(\rho)}{I_0} = e^{-\frac{\rho}{\alpha}}$$

where  $I_0$  is the central luminosity and  $\alpha$  is a constant coefficient called the scale height, representing the radius at which the luminosity is  $I_0/e$ . The luminosity function in the  $z$ -direction, representing the "thickness" of the disk is also given by an exponential function

$$\frac{I_z(z)}{I_0} = e^{-\frac{|z|}{\alpha_z}}$$

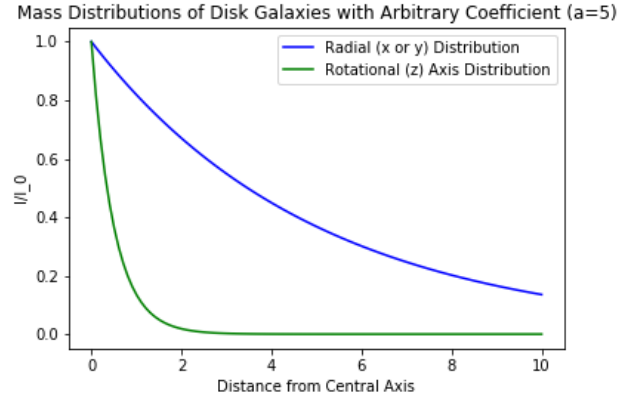


**Figure 3.** Example of exponential luminosity functions for the radial distribution (along  $x$  or  $y$ ) and the axial distribution (along  $z$ , ie. the thickness). Varying the parameter  $a$  will change the rapidity of decay as one goes away from the central axis. The ratio of  $b = 0.1a$  is characteristic of a typical disk galaxy. Distributions of the  $x, y$ , and  $z$  positions of the bodies in the simulation are compared to these distributions with a variety of values for  $a$  to determine the closeness of the shape to a disk structure.

where  $\alpha_z$  is the scale height for the vertical  $z$ -axis direction. For a disk structure, the typical relation between the scale heights is  $\alpha_z = 0.1\alpha$ . An example showing the typical distributions of a disk with arbitrary units and an arbitrary scale height is shown in Figure 3.

The luminosity profile of a disk galaxy implies a similar mass profile (Freeman 1970), so we take this exponential disk profile to be the simplest idealized disk shape for comparison with the distribution of mass in the simulations. In terms of mass, this profile is represented by a surface mass density:

$$\Sigma(\rho) = \Sigma_0 e^{-\frac{\rho}{\alpha}}$$

At each epoch in the simulations, we fit an exponential profile the surface mass density profile distribution in the data.  $\Sigma$  is calculated by creating bins of equal radial width, summing the number of bodies contained within those bins, dividing by the surface area normal to the radius, and projecting that value to the outermost radial position. The resulting surface mass densities are position dependent and are given in units of solar masses per square kiloparsec ( $M_\odot/kpc^2$ ).

## 5 RESULTS

### 5.1 Positions

We examine the positions of the first 100 plotted particles as they evolve over several epochs. In general, the bodies begin to collapse, and we see a beginning of order that resembles structure formation toward the end of the longer simulations. In Figure 4, three runs of the simulations are shown at three points throughout the run, each initialized with the same parameters with the exception of the randomized velocity component. Figure 4a shows a clear collapse to a more compact form, as does Figure 4b. These appear to represent more reasonable starting conditions for the system, from which we expect to see a gravitational collapse into a more recognizable structure over time. Simulation runs initialized at 0 or 2 km/s show this trend in behavior. Figure 4c, however, clearly expands instead of contracting. We discuss this point further in Section 5.3 in reference



to energy considerations. All simulations initialized at 10 km/s mean random velocity exhibit this behavior. Epochs 0, 25, and 50 for each simulation are displayed in the Appendix.

## 5.2 Mass Distributions

In order to monitor the formation of disk-like shapes, we adopt a combination of radial and vertical exponential profiles to represent our simple ideal. By the process described in Section 4.4, the binning of radial and vertical positions allows us to estimate average radial and vertical mass surface densities. These densities are fit to exponential profiles that optimize the parameters to the best fit of the data. We then apply Kolmogorov-Smirnov statistical tests [Peacock \(1983\)](#) to determine the quality of the fit. The null-hypothesis is that the distribution perfectly follows the models profile, so that the KS-metric represents the normalized difference of greatest discrepancy between the data and the corresponding point in the profile. The p-value represents the probability that another measurement will result in an outcome at least as extreme as the fitted-data. In this case it can be interpreted as the likeliness of the result given a true null hypothesis. By examining the structure, fitting the exponential profiles, and tracking the development of the quality of the fit through the Kolmogorov-Smirnov parameters, we track the system's "diskness".

Figures 5-7 shows the three epochs from the three simulation runs whose positions are shown in Figure 4. The evolution of the surface mass density is an important consideration for understanding the shapes formed by the structure, as the objects are compacted to a more orderly profile. The distributions evolve in an interesting fashion, again clearly showing the contraction of the systems initialized at 0 and 2 km/s mean-magnitude randomized velocities. They may be more successfully modeled by a compound function or a Poisson distribution. The observed presence of spheroidal bulges in the central regions of mature spiral galaxies ([Peletier et al. \(2005\)](#)) is an example of a deviation from the exponential profile. This compound distribution described by distinct regions is well-supported in most spiral galaxy studies. The difference here is that the physics of the central bulge of spiral galaxies is significantly more advanced in complexity than our simulation provides. The central regions of most spiral galaxies contain supermassive black holes ([Ghez et al. \(1998\)](#), [Volonteri \(2010\)](#)), and the surrounding bulge is typically comprised of older stars and high-temperature gas. These are some of the additional complexities that we have neglected in our simulation. For these reasons, we do not believe the observed profile in the result of Figure 6 is suggestive of the formation of the type of bulge structure observed to exist in real galaxies.

As discussed in Section 4.4 we expect over time to see these systems to form structures whose shapes are described by exponential profiles with a relation between the scale height of the radial profile and that of the vertical profile, where  $\alpha_z/\alpha = 0.1$ . On the timescales we have simulated, the structures never clearly visually resemble an exponential profile, which is reflected in high KS-metrics and low p-values throughout. In general, these parameters showed mostly static behavior if averaged over the duration of the simulation, neither improving nor worsening to great extents, though there is more of a trend toward slight improvement overall. This is to be expected, since there is a clear trend toward a profile with higher mass at lower distance from the center point in both the radial and vertical profiles. Interestingly, there appears to be a consistent rise in the KS-metric, corresponding to a worsening of fit, around epoch 40 until the end at epoch 50. This effect is seen across the 50-epoch (50,000-step) simulations and is not seen in the 25-epoch runs. The cause of this

is unknown to us and may be made more clear in a simulation of longer duration.

The ratio  $\alpha_z/\alpha$  does not appear to approach the target value of 0.1, instead almost exclusively increasing monotonically throughout the duration of the simulation, as shown in Figures 5-7. In any case, the relatively poor fits for the majority of profiles and distributions makes the  $\alpha$  parameter from those simulations less helpful in describing the actual flattening of the disk shape. It does appear that these systems are not approaching the exponential disk profile we expect, at least in the timescales we have simulated. As with many questions, a longer simulation may provide more evidence to support or refute our expectations.

## 5.3 Energy

Results on the energy from the data are tenuous. Magnitudes of the kinetic and potential energy monotonically increased for all of the simulations except for the ones that were initialized at the highest random velocities (mean 10 km/s). We note that high initial velocities correspond to high initial kinetic energies that may overcome the gravitational potential well and escape. For higher initial velocities, then, we expect to see very little structure formation on the timescales we are simulating. These points are shown also in the contracting or expanding of the positions of the objects in Figure 4.

The simulations initialized at a small but nonzero randomized velocity (2 km/s) appear to more smoothly and reasonably approach the condition of a virialized system. At 25 epochs (2.5 Gyrs), the ratio of potential energy to kinetic energy has decreased below 10, and by 50 epochs (5 Gyrs) it has reached a value of 5. For the evolution of the system on cosmological timescales, this would suggest that the system would approach the virial condition within the following 2-3 Gyrs. At an age of 7-8 Gyrs, around half the age of the universe, this system may be approaching this state of stability as the star-formation cycle begins to have a significant effect on the dynamics of the system. Given more steps, these parameters may approach and oscillate about an equilibrium of energy and show a structure more recognizable to our intuitions.

The rotational component of the initial velocity appears to have comparatively little effect on the behavior of the time-evolution of the potential and kinetic energy curves. We believe a range of greater initialized angular velocities will introduce more variation.

# 6 DISCUSSION

## 6.1 Additional Complexities

Galaxy formation is an incredibly complicated process that results from multiple systems interacting at high energy levels across vast distances and over extreme time periods. Current galaxy formation simulations contain initial states of dark matter which dominate the mass of the protogalaxy. These pockets of dark matter are believed to the seeds that the galaxies grow out of, as virtually all galaxies have been observed to contain halos of dark matter around them. The baryonic matter will condense around the pockets of dark matter, making dark matter a fundamental galaxian requirement.

Collisional physics is also included in many galaxy formation simulations as gas clouds and stars will meet and influence each other's momentum and therefore the morphology of the galaxy. Thermodynamic and magnetization properties of gas clouds affect the morphology of the protogalaxy, as well as supernovae feedback, change in mass by star formation, and star formation lifetime.

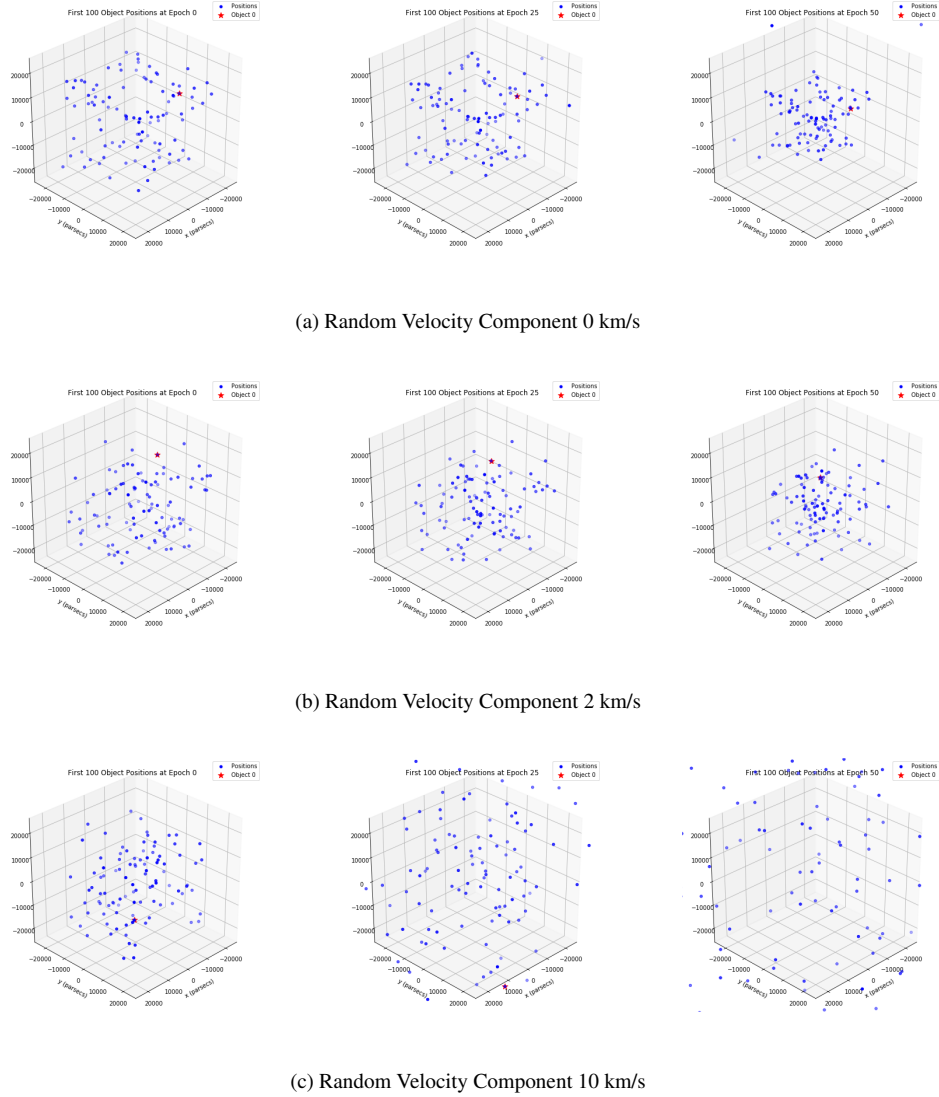


**Figure 4.** Positions for beginning, middle, end of 50 epochs. 0, 2, and 10 km/s.

The complexity does not stop there, though these are predominant components of current large scale simulations.

In galaxy simulations of greater scale, galaxy formation is usually described in two differing scenarios: "top-down" and "bottom-up". In a "top-down" scenario the initial clouds of gas and dark matter collapse and most or all of the gas turns into stars and the morphology of the galaxy remains mostly unchanged and is affected only by the formation rate of stars within the galaxy. The "bottom-down" scenario is where several protogalaxies, where not all of the gas has fused into stars, coalesce and merge into a larger galaxy.

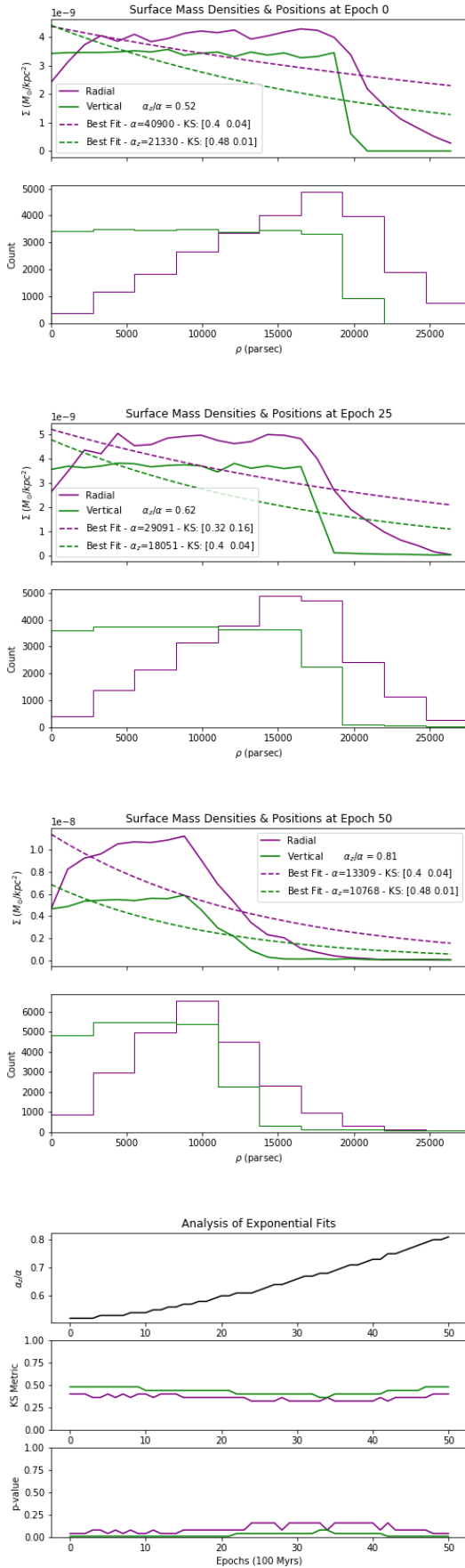
Evidence in the form of extremely red-shifted quasars suggests that both of these models are correct. In the early universe, less than one billion years old, large gas clouds formed large galaxies with extreme luminosity. However, *giant* galaxies are much more common after a few billion years. This shows that galaxies can form in different ways under different circumstances, and that small changes in initial conditions have very large effects of the final morphology of a galaxy after billions of years of evolution.

## 6.2 Selected Complexity

The processes that govern the creation and evolution of a galaxy are extremely complex, however, they can be modeled by a simplistic equation at the expense of accuracy. By only simulating the force of gravity, the morphology of the galaxy can be calculated as the simulation runs by relating the kinetic and potential energies.

Due to the limits of processing power, the scope of this simulation is the gravitational interaction of uniform bodies with varied initial velocities. We expect these bodies to initially expand outwards before succumbing to the gravitational potential and being pulled back in. As these bodies approach the center of mass of the system, their kinetic energy will increase as their gravitational potential energy decreases. These bodies will then pass the center of mass before again being pulled in the opposite direction. The ratio of kinetic energy to potential should oscillate until the bodies reach stable orbits and begin to move as a more cohesive disk, rotating around the center of mass.

The morphology of this disk should vary greatly with the time scale of the simulation. As the simulation runs longer, more bodies



MNRAS **000**, 1–12 (2020) **Figure 5.** Random Velocity Component 0 km/s

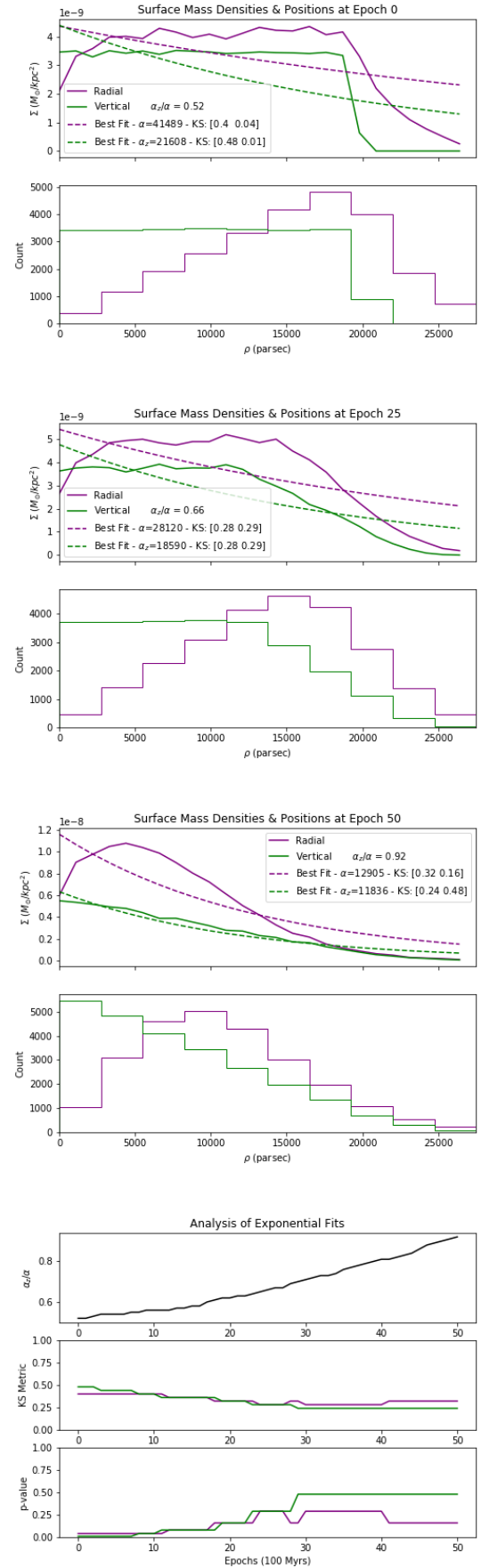


**Figure 6.** Random Velocity Component 2 km/s

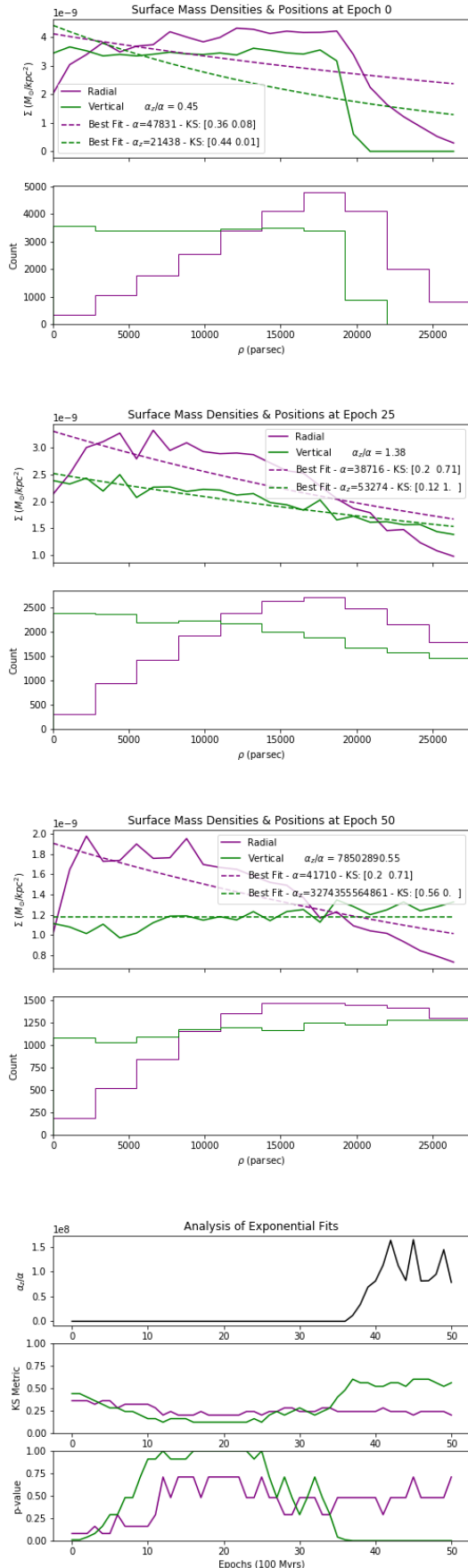


Figure 7. Random Velocity Component 10 km/s

will interact gravitationally and pull the outliers into the average direction. Given enough run time, all bodies should eventually form a stable, circular orbit around the center of mass in a flattened, disk-like shape. However, if the bodies' initial velocity is too great to be forced inward by gravity, the masses will never coalesce.

### 6.3 Initial Conditions

When first starting the simulations, our expectations for the initial conditions needed to be altered. Namely, the mean random velocity of each body proved to be too high. After running early simulations, it was clear that the gravitational force was not able to "overcome" the mean random velocities we had originally chosen in a realistic time table. Originally, we had expected random velocities to 10 km/s to 100 km/s to be physically appropriate for the system. However, after some testing, random velocities on the scale of 0 km/s to 10 km/s were more appropriate, with even 10 km/s showing little to no coalescence in the time scale simulated. Further testing with more granular values of random velocity in the 1 km/s to 10 km/s would yield interesting results relating to the limit of random velocities and the amount of time it would take bodies with those random velocities to coalesce.

As well as the mean random velocities, our expectation of initial mass density in the simulation area was adjusted. To aid the simulation in producing results over the times simulated, a larger over density of mass was needed, thereby increasing the average gravitational force acting on each body. In the end, a total mass an order of magnitude higher than what originally predicted was used. This effectively "sped up" the simulation while still remaining physically plausible. Further simulations with varied mass densities over a longer simulation time would prove an interesting area of research.

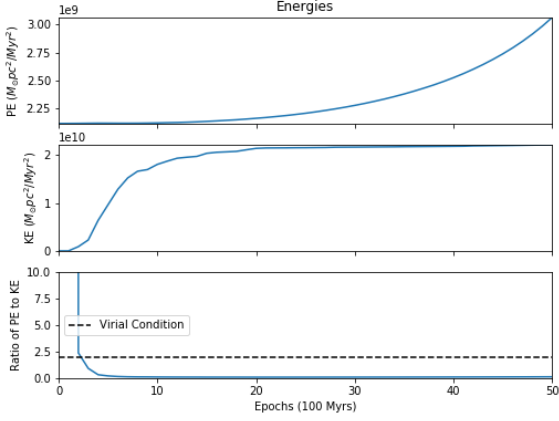
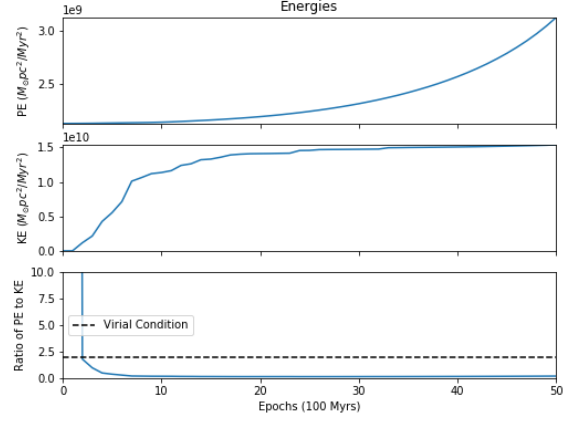
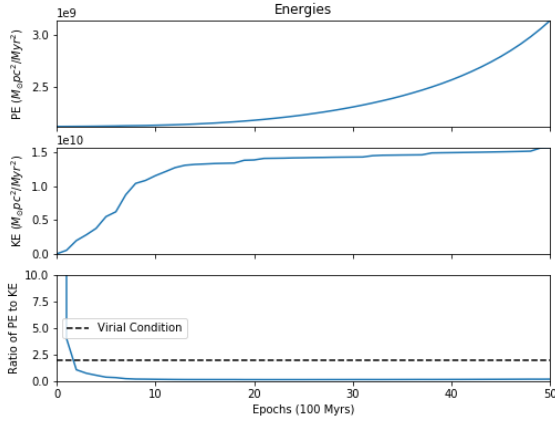
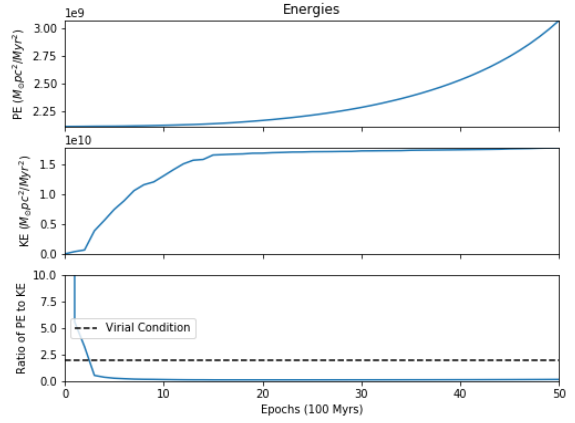
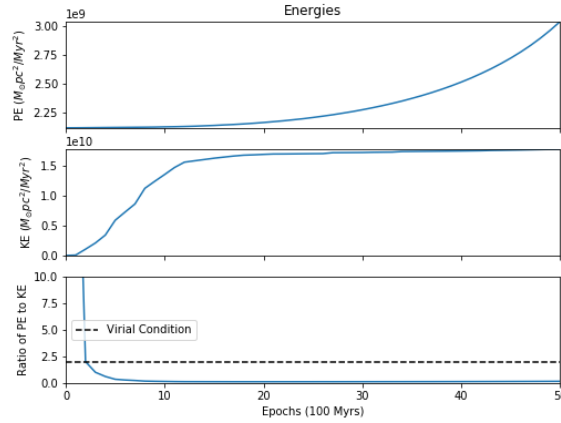
### 6.4 Algorithm Analysis

In a broad sense, the algorithm employed proved reasonably successful. Compared to a "brute-force" algorithm, where forces are calculated between each pair of bodies, our algorithm was significantly faster. While the brute-force method took approximately 3-4 hours to simulate 1000 bodies for 25,000 steps, our algorithm was able to run the same simulation with 25,000 bodies in a similar amount of time.

Our algorithm, however, did have some limitations. The most obvious of these being the single threaded nature of the simulation. While parallel processing does add much more complexity, the results allow for simulations to be run on a far larger scale. Currently, the main computational cost for each step is from the calculation of force. Due to the dependent nature of the tree structure, a simple parallel implementation of the algorithm would generate the tree in a single process before splitting up the work between all processes when calculating the forces acting on each particle. A simple parallel implementation following this outline was attempted, before being aborted due to time concerns.

Regarding the solution to artifacting, our approach was reasonably successful. As described previously, when the distance between the subject and actor were too close, a minimum distance was used rather than the actual one. From our visualizations, some artifacting was clear, but only mainly detectable in the 0 km/s mean random velocity case. However, this appeared to happen to a proportionally small number of bodies when compared to the total number of bodies, leading us to believe it did not significantly impact our results.

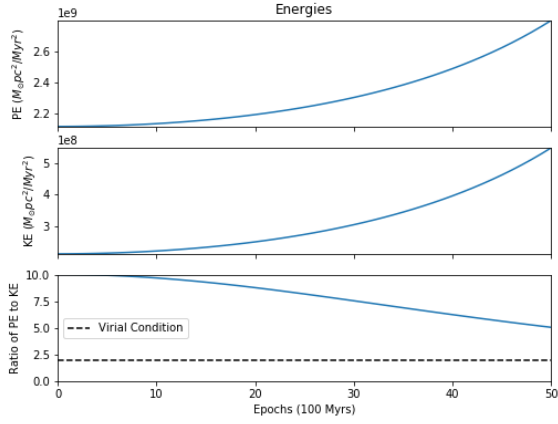
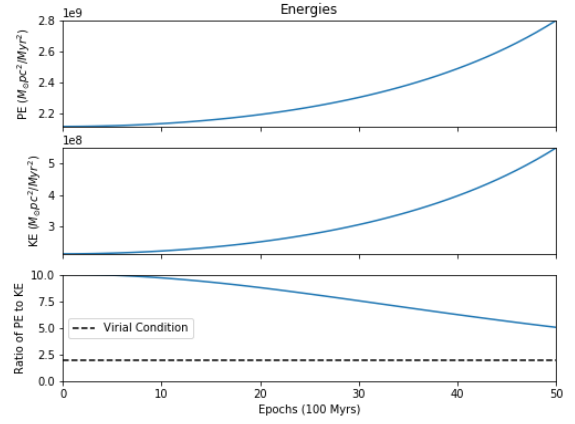
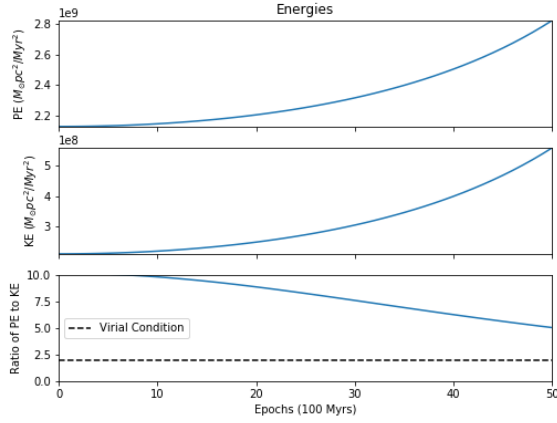
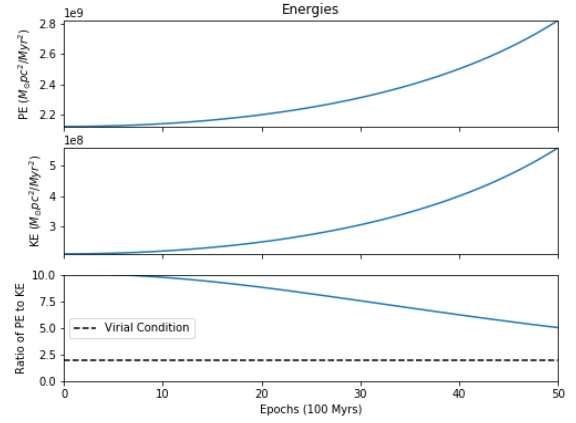
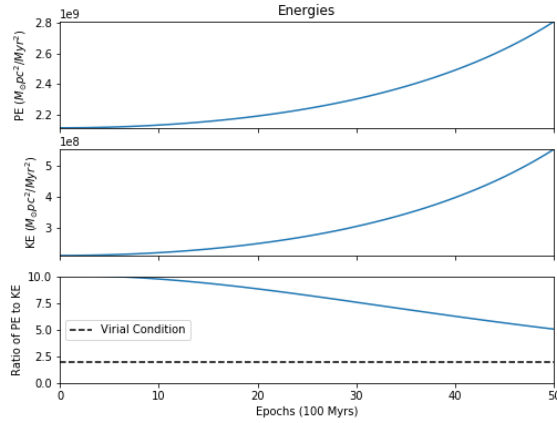


(a)  $\Omega = 0.1$  rad/Gyr(b)  $\Omega = 0.15$  rad/Gyr(c)  $\Omega = 0.2$  rad/Gyr(d)  $\Omega = 0.25$  rad/Gyr(e)  $\Omega = 0.30$  rad/Gyr

Despite its simplicity, this method may prove to have physical merits, as two bodies approaching closely would "orbit" one another, rather than collapse to a distance of zero. This orbit distance could be modeled by the softening factor chosen. To improve this method, much more testing would have to be done to determine a more appropriate softening factor.

A small consideration when running the simulations was the

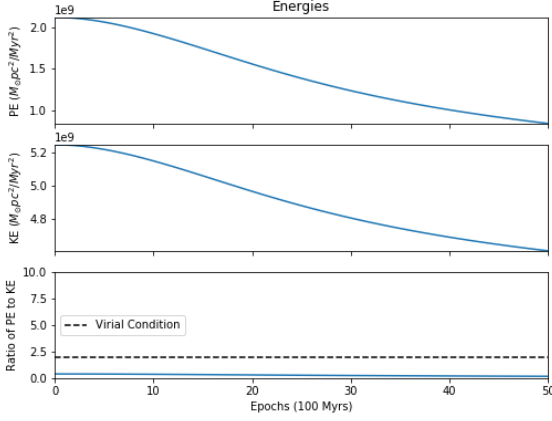
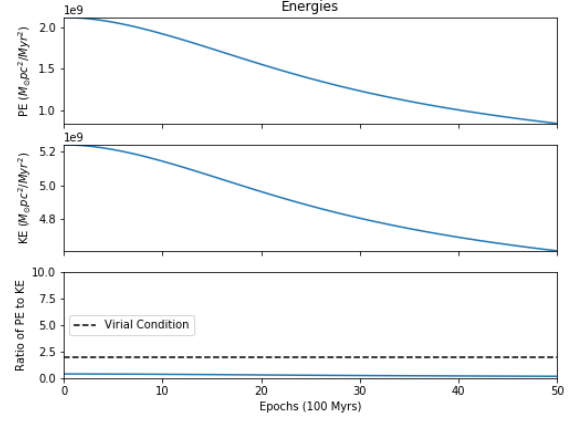
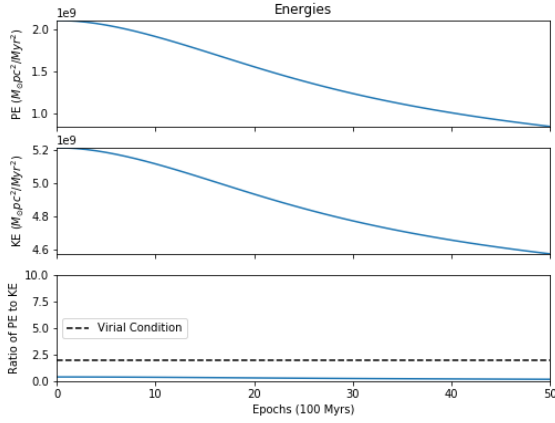
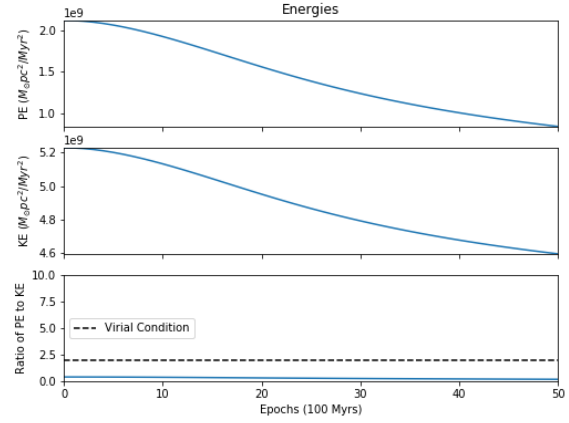
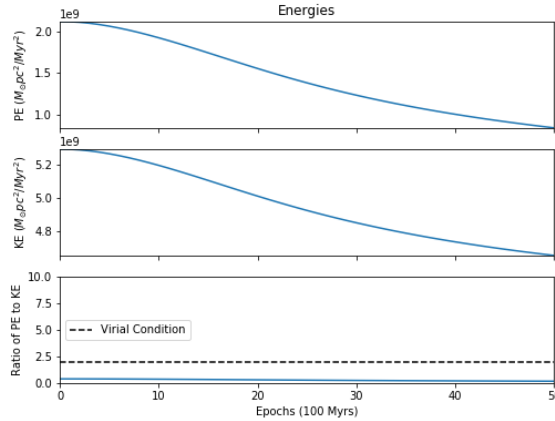
method of seeding the random function. Because the seed used for the random number generator was the current time, care must be taken when starting the simulations. While tempting to run the simulations in large batches, there must be a delay between when each simulation is run in order for the positions and velocities to actually be randomized. A solution to this may have been to seed the random function every time a new particle is initialized, but a

(a)  $\Omega = 0.1$  rad/Gyr(b)  $\Omega = 0.15$  rad/Gyr(c)  $\Omega = 0.2$  rad/Gyr(d)  $\Omega = 0.25$  rad/Gyr(e)  $\Omega = 0.30$  rad/Gyr

simple script to delay the execution of each simulation is arguably more effective.

The final limitation in our algorithm was keeping precision in calculations. When performing multiplications and divisions with small and large numbers, precision can be "lost" through floating point errors and numbers effectively equaling zero. This resulted in simulations where very little apparent movement occurred, and with

very small changes in kinetic and potential energies. To mitigate this, we chose to represent energies in terms of solar masses, parsecs, and mega years, to avoid "lossy" calculations when converting to SI units.

(a)  $\Omega = 0.1$  rad/Gyr(b)  $\Omega = 0.15$  rad/Gyr(c)  $\Omega = 0.2$  rad/Gyr(d)  $\Omega = 0.25$  rad/Gyr(e)  $\Omega = 0.30$  rad/Gyr

## 7 CONCLUSIONS

We arrive at a few key conclusions based on the data output by the simulations:

(i) **The initial parameter governing the distribution of the magnitudes of randomized velocity components exhibits a significant effect on the resulting behavior of the system.**

- Low, non-zero randomized velocity components (2 km/s in our simulation) result in the most reasonable energy and structural evolutions with respect to our expectations. This is the optimal parameter range for future studies.

- Higher randomized velocity components (10 km/s in our simulation) result in particles exceeding the escape velocity and

a general expansion of the system, instead of the expected contraction.

(ii) **On the other hand, the range of rotational velocities we employed appear to have little effect on the resulting structure and energy considerations.**

- Future studies should include higher angular velocities for more understanding of parameter space that may introduce variations to the output.

(iii) **The energies did not converge to an equilibrium at the ratio specified by the virial theorem in the timescales of our simulation.**

- Notably, the most promising simulation runs appear to suggest an approach of this ratio given around 50% more time.
- The energies reflect the conditions of contraction or expansion that are shown in the positions and mass distributions.

(iv) **The surface mass distributions did not approach the exponential disk profiles of our model fits in the timescales of our simulation.**

- The most promising simulation runs appear to approach interesting profiles that may be better fit given longer time or a different test profile.

An extension of this simulation's direction and goals with additional complexities and longer timescales, with the refinement of reasonable parameter space for initial conditions, may yield interesting insights to disk structure formation. This project has provided a useful first roadmap for the navigation of the subject.

## 8 ACKNOWLEDGEMENTS

AT would like to thank his lovely hair. SK would like to thank AT. TW would like to thank his mom.

We used these software packages: python, sciPy, astroPy, numPy, Pandas, etc. etc. etc.

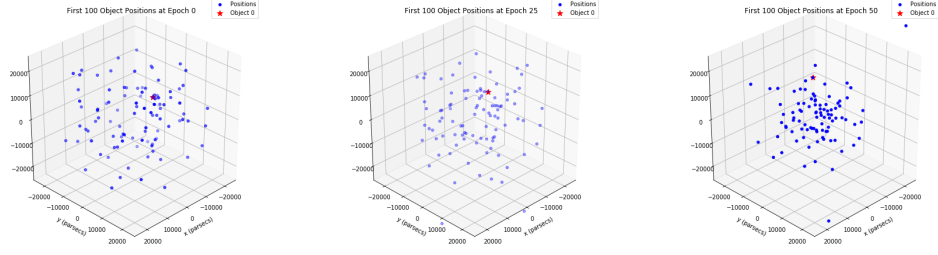
## REFERENCES

- Barnes J., Hut P., 1986, *Nature*, 324, 446  
 De Lucia G., Springel V., White S. D. M., Croton D., Kauffmann G., 2006, *MNRAS*, 366, 499  
 Eggen O. J., Lynden-Bell D., Sandage A. R., 1962, *ApJ*, 136, 748  
 Freeman K. C., 1970, *ApJ*, 160, 811  
 Ghez A. M., Klein B. L., Morris M., Becklin E. E., 1998, *ApJ*, 509, 678  
 Holmberg E., 1941, *ApJ*, 94, 385  
 Hubble E. P., 1926, *ApJ*, 64, 321  
 Hubble E. P., 1927, *The Observatory*, 50, 276  
 Illingworth G. D., et al., 2013, *ApJS*, 209, 6  
 Ostriker J. P., Peebles P. J. E., Yahil A., 1974, *ApJ*, 193, L1  
 Peacock J. A., 1983, *MNRAS*, 202, 615  
 Peletier R., Balcells M., Falcon-Barroso J., Graham A., 2005, arXiv e-prints, [pp astro-ph/0502286](#)  
 Sofue Y., Rubin V., 2001, *ARA&A*, 39, 137  
 Volonteri M., 2010, *A&ARv*, 18, 279  
 White S. D. M., 1976, *MNRAS*, 177, 717  
 White S. D. M., Sharp N. A., 1977, *Nature*, 269, 395  
 Williams R. E., et al., 1996, *AJ*, 112, 1335

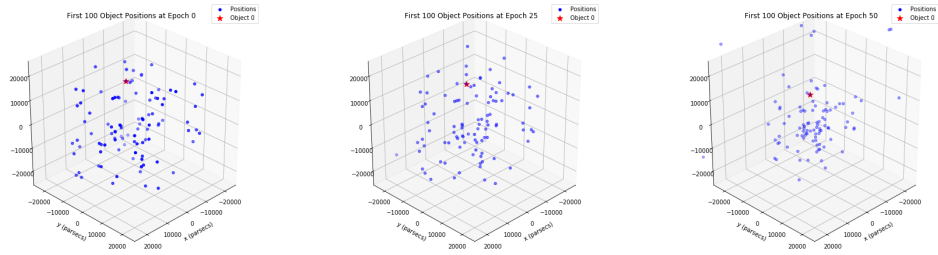
## APPENDIX A: POSITIONS

Below are the positions of the first 100 objects placed and tracked over 50 epochs, shown here in increments of 25 epochs, where  $\Omega$  is the initial total angular velocity.

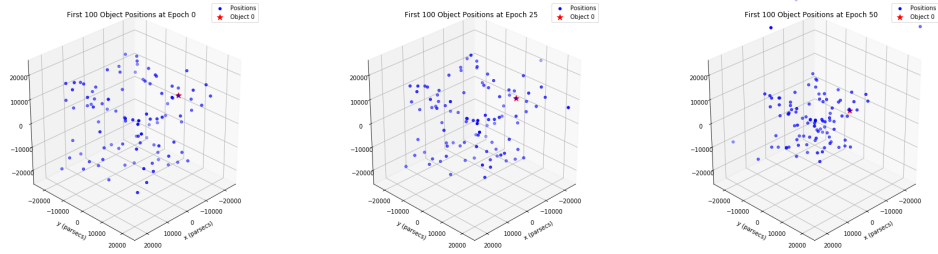
This paper has been typeset from a  $\text{\LaTeX}$  file prepared by the author.



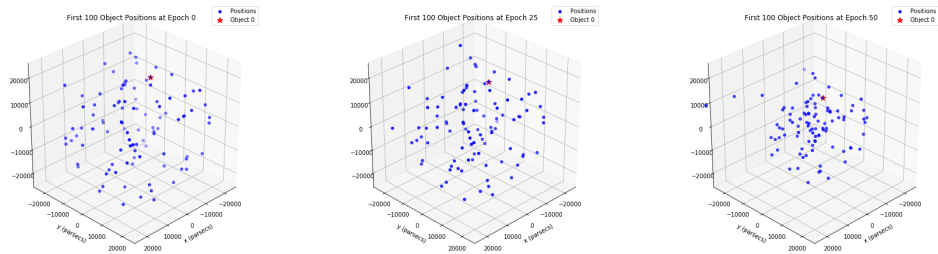
**Figure A1.** Random Velocity Component 0 km/s,  $\Omega = 0.1$  rad/Gyr



**Figure A2.** Random Velocity Component 0 km/s,  $\Omega = 0.15$  rad/Gyr

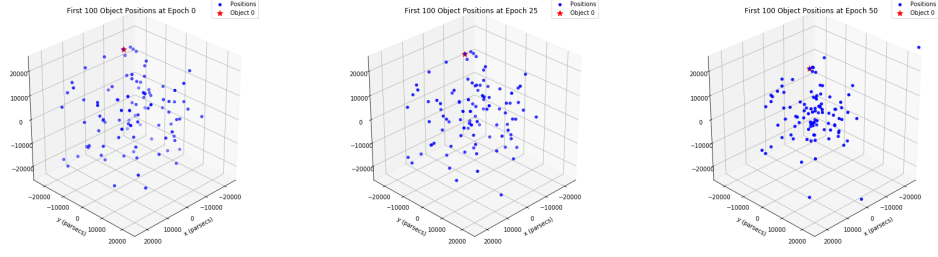
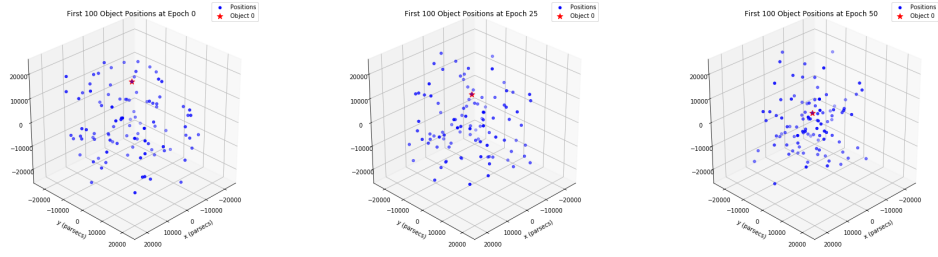
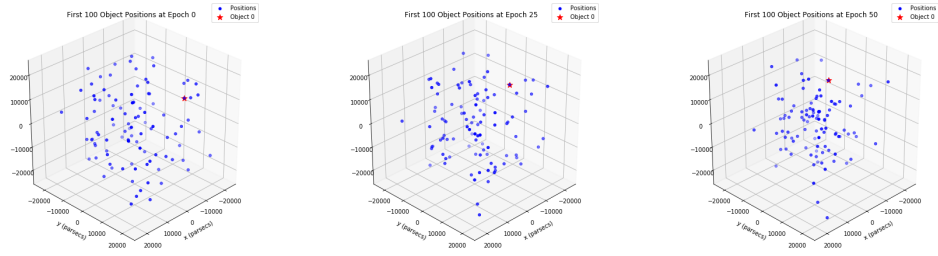
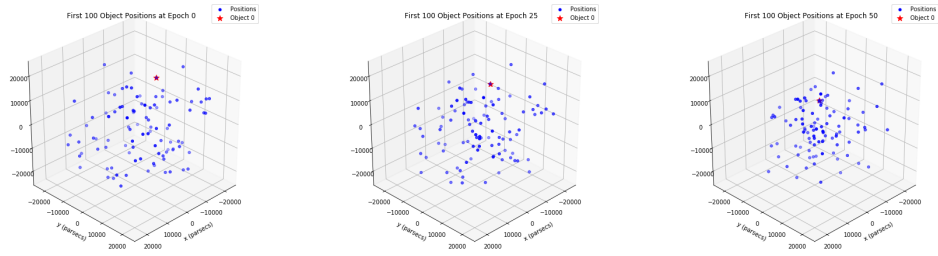


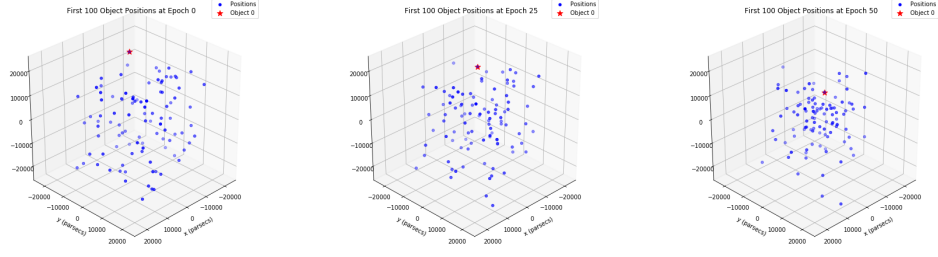
**Figure A3.** Random Velocity Component 0 km/s,  $\Omega = 0.2$  rad/Gyr



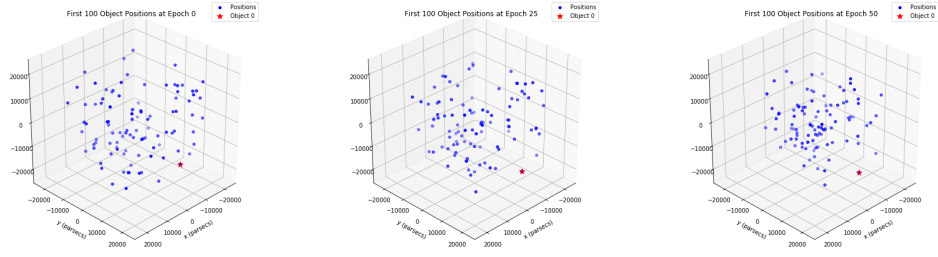
**Figure A4.** Random Velocity Component 0 km/s,  $\Omega = 0.25$  rad/Gyr



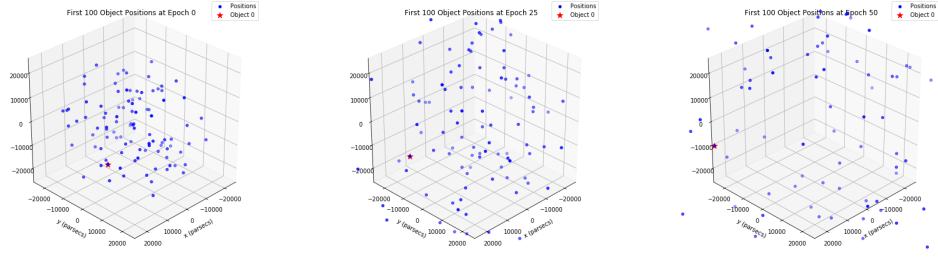
**Figure A5.** Random Velocity Component 0 km/s,  $\Omega = 0.3$  rad/Gyr**Figure A6.** Random Velocity Component 2 km/s,  $\Omega = 0.1$  rad/Gyr**Figure A7.** Random Velocity Component 2 km/s,  $\Omega = 0.15$  rad/Gyr**Figure A8.** Random Velocity Component 2 km/s,  $\Omega = 0.2$  rad/Gyr



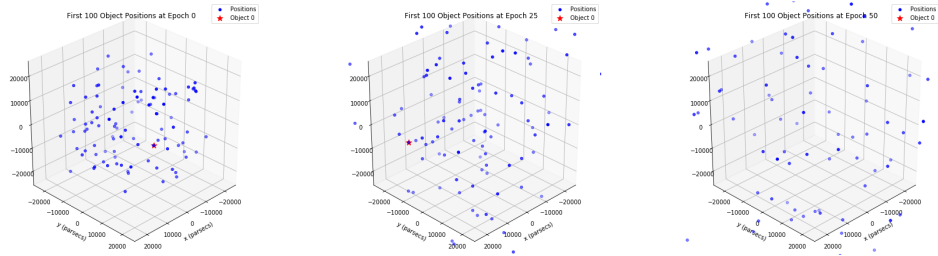
**Figure A9.** Random Velocity Component 2 km/s,  $\Omega = 0.25$  rad/Gyr



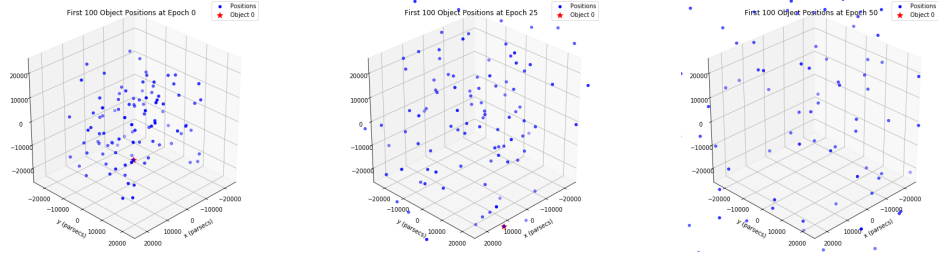
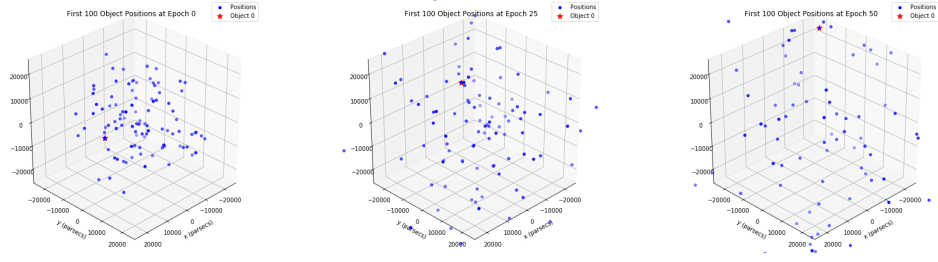
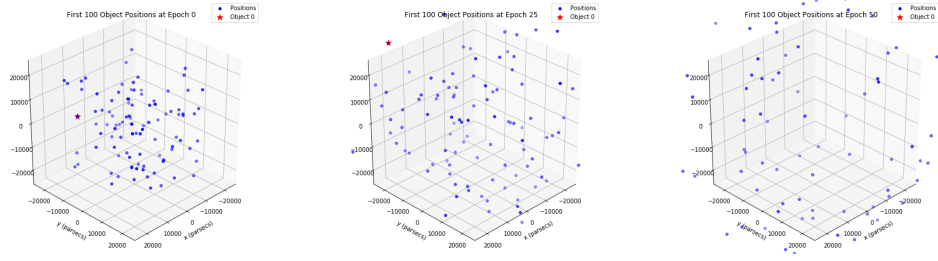
**Figure A10.** Random Velocity Component 2 km/s,  $\Omega = 0.3$  rad/Gyr



**Figure A11.** Random Velocity Component 10 km/s,  $\Omega = 0.1$  rad/Gyr



**Figure A12.** Random Velocity Component 10 km/s,  $\Omega = 0.15$  rad/Gyr

**Figure A13.** Random Velocity Component 10 km/s,  $\Omega = 0.2$  rad/Gyr**Figure A14.** Random Velocity Component 10 km/s,  $\Omega = 0.25$  rad/Gyr**Figure A15.** Random Velocity Component 10 km/s,  $\Omega = 0.3$  rad/Gyr